RESEARCH ARTICLE

On the UOWC Performance Under Location Uncertainty

NICHOLAS VAIOPOULOS[1], **ALEXANDER VAVOULAS**[1], **HECTOR E. NISTAZAKIS**[2],
HARILAOS G. SANDALIDIS[1], **AND ATHANASIOS KAKAROUNTAS**[1], (Senior Member, IEEE)

[1]Department of Computer Science and Biomedical Informatics, University of Thessaly, 35131 Lamia, Greece
[2]Department of Physics, National and Kapodistrian University of Athens, 15784 Athens, Greece

Corresponding author: Athanasios Kakarountas (kakarountas@dib.uth.gr)

ABSTRACT More often than not, currents due to gravity, wind friction, and heterogeneous water density cause frequent drifts of the end-users to random locations creating transmission problems in an underwater optical wireless communication (UOWC) network. The location uncertainty effect on the overall network performance in harsh environments, including submarine ones, is an appealing issue that needs to be adequately addressed in the existing technical literature. The present work takes account of a vertical UOWC link where a fixed transmitter at the sea surface illuminates towards the seabed following a Lambertian pattern. In this way, a randomly placed receiver inside a spherical cone is served, and the problem is treated with three-dimensional stochastic geometry methods. In the sequel, the complete statistical behavior of the random distributions of the channel gain and the instantaneous electrical signal-to-noise ratio is estimated. Moreover, some critical network performance metrics, including the outage probability and the bit-error rate for intensity modulation/direct detection with on-off keying and M-ary pulse position modulation, are derived, whereas indicative numerical results are illustrated adequately through a series of appropriate figures.

INDEX TERMS UOWC communications, random location, spherical conical volume.

I. INTRODUCTION

A. PRELIMINARIES

The profusion of scientific work on underwater optical wireless communication (UOWC) networking, as documented in the extensive surveys by [1] and [2] and the recent review by [3], testifies to the highly increased influence of this technology in the digital era of tomorrow. UOWC, which normally operates in the blue-green (450-532) nm wavelength spectrum, has evolved as a complementary candidate compared to traditional acoustic communications, given its ability to provide high data rates with low latency. These two features offer significant advantages to these systems regarding

their massive exploitation in deploying the so-called internet of underwater things (IoUWT), particularly in subsea environments. IoUWT aims to render some appealing real-time applications such as those aptly mentioned by [3], including, among others, ocean floor bathymetry, underwater environmental monitoring, navigation and surveillance, naval-mine reconnaissance, border and coastal security, as well as seismic monitoring and ocean sampling.

However, submarine environments are the least explored areas of the planet, which makes optical signal transmission a challenging issue for telecommunications engineers. Optical signals can propagate only a few tens of meters due to the high attenuation degree, and therefore an adequate trade-off between depth and coverage is necessary for estimation in vertical UOWC links, as pointed out in [4]. Besides, several

additional effects hinder their performance, including pointing errors between transmitter (Tx) and receiver (Rx) [5], [6], random air-bubble generation created by breaking waves [7], sea surface slopes for links near the sea surface [8], vertical salinity gradient [9], and turbulence appearance [10], [11]. In addition, currents generated by gravity, wind friction, and heterogeneous water density often move the end-user terminals to random locations, so pointing and tracking mechanisms should be considered as outlined in [12]. With this in mind, the location uncertainty was recently addressed in two dimensions (2D) for a UOWC vertical link in [13], where a node was randomly placed in a circular coverage area at a certain depth. Roughly speaking, problems of this kind are the subject of the stochastic geometry field, also known as a geometrical probability in the old days [14], [15].

B. LITERATURE REVIEW

It is clear that the investigation of uncertainty in three dimensions (3D) increases complexity but leads to safer conclusions about the impact of this phenomenon. In view of the above, recent applications of stochastic geometry to 3D problems appeared in the open technical literature. Some denotative studies, among others, include the following. In [16], a mixed mobility model for a 3D unmanned aerial vehicle network (UAV) with cylindrical geometry was explored. Using this model, the authors focused on the coverage probability of a user equipment (UE) in a finite network of UAVs under different UAV association policies. The authors also considered the impact of interference from nonserving UAVs on the coverage probability of the UE. In [17], Talgat et al. assumed a system with several concentric spheres, each containing a number of points uniformly distributed on their surface, and employed stochastic geometry to provide a new tractable model for distance distributions with emphasis on satellite networks. In [18], the authors assessed the downlink performance for uniform distribution for satellites in a low-earth-orbit (LEO) network. They developed analytical expressions for the downlink coverage probability and average data rate using stochastic geometry tools. The proposed model and analysis provided guidelines for selecting design parameters for massive LEO constellations, such as the number of frequency channels and altitude.

Very recently, the random placement within a truncated cone with applications to UAV communications and indoor visible-light communications (VLC) was thoroughly analyzed in [19] and [20], respectively. In the first study, the authors derived closed-form expressions for the probability density function (PDF) and cumulative distribution function (CDF) of the random distance from the apex to a random point placed in a truncated conic shape with applications in UAV to UAV communications. In the second one, the authors focused on the VLC channel gain and then evaluated the outage probability and average bit error rate (BER) for on-off keying (OOK) under single-user and multi-user scenarios, considering intensity modulation/direct detection (IM/DD).
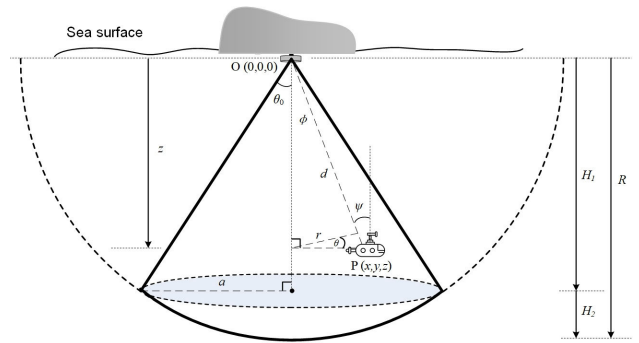

FIGURE 1. System configuration.

C. MOTIVATION

Similar to the aforementioned, a 3D stochastic geometric analysis of the location uncertainty issue in the case of a UOWC requires adopting a relatively realistic geometric coverage model. The model must be suitable for the homogeneous propagation medium, incorporate the environment characteristics, and have a convenient mathematical description to facilitate the overall performance evaluation. In the case of our UOWC scenario, some candidate models include the sphere [21] or the hemisphere due to the uniformity (constant radius) in all directions. In the event of a UOWC link, the hemisphere seems appropriate at first sight since the Tx is located at the sea surface. However, upon careful observation, one can observe that neither hemisphere reflects reality as the Rxs rarely lie near the surface. Furthermore, such consideration would require light-emitting diodes (LEDs) with high irradiance angles and emission power to support communication links inside the hemispheric volume. In this respect, Txs with low irradiance angles must be used, and in this case, the coverage volume takes the shape of a spherical cone. Notwithstanding, to the best of our knowledge, the consideration of position uncertainty in a spherical conical volume with application to UOWC has not been addressed to date, which motivated our interest in conducting the present study.

D. MODEL DESCRIPTION

Without loss of assumption, the mathematical analysis presumes the system configuration in Fig. 1, which refers to a vertical UOWC link with a fixed Tx located at the sea surface and considered as the axis origin, O. The Tx comprises a single LED or a LED array directed toward the seafloor. The emission follows a Lambertian radiation pattern, thus illuminating the spherical conical coverage volume whose surface is marked in a bold black line and determined by the semi-angle θ_0. The Tx semi-angle at half luminance is denoted by $\phi_{1/2}$ and is the angle from the axis perpendicular to the LED by which the luminous intensity is only 50%. It should be noted that the values of θ_0 and $\phi_{1/2}$ are not necessarily equal. An optical Rx is randomly placed at point P with Cartesian $\{x, y, z\}$ and cylindrical $\{r, \theta, z\}$ coordinates,

respectively. The incidence angle is denoted by ψ whereas the Euclidean distance between Tx and Rx is d. Moreover, the critical geometric parameters (radius R of the underlying hemisphere, distances H_1 and H_2, and radius α) are distinctly depicted.

E. CONTRIBUTIONS

In summary, the paper fills the void of relevant studies in the technical literature regarding the effect of terminal uncertainty within a spherical conical coverage volume, and its contribution includes the following points:

- We focus on the location uncertainty of the receiver (Rx) and expand the model from 2D to 3D to obtain a more realistic assessment of performance. By doing that, the coverage volume is represented by a spherical conic shape, and we also consider the particular case of a hemispherical shape. This extension allows us to consider the additional depth dimension, resulting in a more accurate representation of the real-world scenario

- We assess the efficiency of a UOWC system in which the location of the receiver (Rx) is uniformly dispersed inside a spherical conic volume. To accomplish this, we derive an analytic expression for the joint PDF of the radical distance and height of a point uniformly placed within the spherical cone. Utilizing this expression, we can derive novel closed-form expressions for the complete statistical behavior of the random channel gain for a depth-dependent extinction coefficient, which measures the signal's attenuation as it travels through the water. These expressions enable us to accurately estimate the performance of the UOWC system under different conditions.

- We derive analytic mathematical formulas for the PDF and CDF of the instantaneous electrical signal-to-noise ratio (SNR). These formulas allow us to analyze the SNR and understand its behavior mathematically. In addition to the derived formulas, we also use Monte Carlo (MC) simulations to validate our results. By comparing the results obtained from the analytic formulas with those obtained from the MC simulations, we can ensure the accuracy and reliability of our analysis.

- In conclusion, we mathematically deduce the outage probability and compute the average BER for OOK and M-ary pulse position modulation (M-PPM) schemes under the assumption that the receiver uses intensity modulation/direct detection (IM/DD). We examine the most crucial factors using relevant figures to analyze the influence of different link parameters on the overall performance.

F. STRUCTURE

Beyond the introductory chapter, the rest of the paper is structured as follows. Section II outlines the fundamental assumptions of the channel model employed throughout the study. These considerations provide the basis for interpreting the results obtained in the subsequent sections of the paper. Section III deals with the theoretical analysis of the uncertainty problem. The primary statistical metrics of the random channel gain versus Tx-Rx distance and SNR are extracted in closed-form mathematical expressions. Section IV evaluates the outage probability and average BER of the examined UOWC link. The analysis yields important insights into the performance and reliability of the link under various conditions. Representative results are adequately discussed. Eventually, Section V offers a brief overview of the key findings and implications of the work, highlighting the contributions and significance of the study. It also discusses potential directions for further research and development.

II. CHANNEL MODEL
A. EXTINCTION COEFFICIENT MODEL

Seawater contains large amounts of dissolved or suspended elements in various concentrations and chlorophyll, which is the pigment used by phytoplankton to capture and convert solar energy into biomass. This composition activates two physical processes that contribute decisively to the degradation of the transmitted optical signal along the light path, namely absorption and scattering, which are affected by both wavelength and depth. Therefore, if λ is the wavelength of light when traveling in a vacuum, the extinction coefficient, $c(\lambda, L)$, at a specific depth, L, is determined by the sum of absorption, $a(\lambda, L)$, and scattering coefficient, $b(\lambda, L)$ as [22]

$$c(\lambda, L) = a(\lambda, L) + b(\lambda, L). \tag{1}$$

These two factors have extensively been considered in the open technical literature and can further be analyzed and calculated by the sum of individual coefficients referring to specific absorption and scattering characteristics [23]. Therefore, from (1) one can readily estimate the extinction coefficient at any depth and operating wavelength values. However, since this value does not take L into account, we make use of the average extinction coefficient denoted by $c_{av}(\lambda, L)$ which occurs by integrating the extinction coefficient over the total depth as [13]

$$c_{av}(\lambda, L) = \frac{1}{L} \int_0^L c(\lambda, x) dx. \tag{2}$$

Note that the chlorophyll concentration varies from sea level to a depth of L. A peak in chlorophyll concentration has been observed due to an optimal trade-off between sunlight and nutrients, occurring at a depth between 20m and 120m [24]. Based on extended measurements, the chlorophyll concentration over a depth L was modeled as a five-parameter Gaussian curve in [24], and nine profiles (also called S profiles) have been assumed to represent different ocean locations. Therefore, the average extinction coefficient can be estimated for each of these profiles, as illustrated adequately in Fig. 2. It is clear that as we pass from profile $S1$ to profile $S9$, the average extinction coefficient values on the vertical axis increase, indicating a more hostile environment for the propagating light.
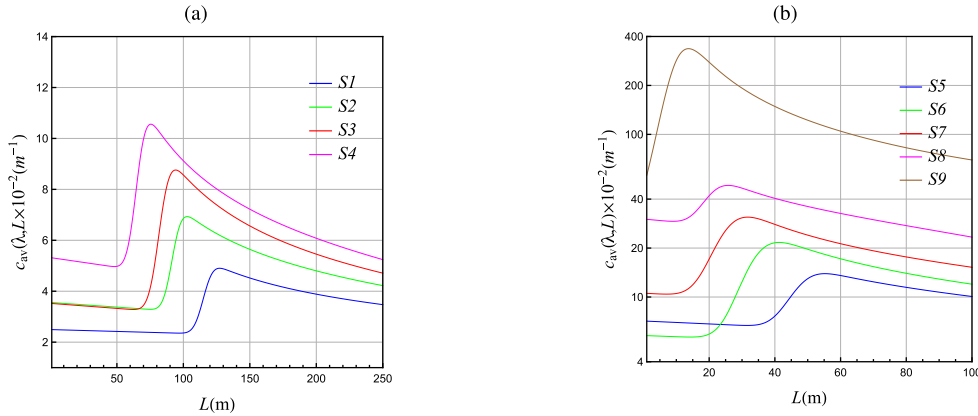
FIGURE 2. Average extinction coefficient for (a) S1–S4 and (b) S5–S9 profiles.

Incorporating (2) in the channel gain model is critical in a vertical underwater optical link. The quantification of losses and the corresponding performance analysis considers the fundamental physical mechanisms governing light propagation in the underwater environment, thus enhancing the validity of the obtained results. In the current study, we chose S2 and S5 profiles, which have small and moderate values of the average extinction coefficient, respectively, as the most representative of a typical underwater environment [13].

B. CHANNEL GAIN

For the assessment of the channel gain, h, we follow the recently published generic model in [5] which refers to line-of-sight (LOS) conditions

$$h = \frac{(m+1)\cos^m(\phi)A_{\text{eff}}}{2\pi d^2} e^{-dc_{\text{av}}(\lambda, L)}, \qquad (3)$$

where ϕ is the Tx irradiance angle, m is the order of the Tx Lambertian emission given by

$$m = -\frac{\ln 2}{\ln(\cos(\phi_{1/2}))}, \qquad (4)$$

where A_{eff} is the effective Rx light collection area expressed as

$$A_{\text{eff}} = \frac{A_{\text{PD}}T_s(\psi)\cos(\psi)n^2}{\sin^2(\phi_{\text{FoV}})}. \qquad (5)$$

In the above equation, A_{PD} is the active photodetector (PD) area, $T_s(\psi)$ the average filter transmission over the filter wavelength range $\Delta\lambda$ for a specific incidence angle ψ [25], n is the refractive index and ϕ_{FoV} is the Rx field of view (FoV). Without loss of generality, we consider that the Tx and the Rx planes are parallel, i.e., $\psi = \phi$.

III. STATISTICAL METRICS
A. JOINT PDF

As a first step, the joint PDF of a random point location inside the spherical cone of Fig. 1 is derived according to the following lemma.

Lemma 1: The joint PDF of the radical distance and height of a uniformly located point inside the spherical cone of Fig. 1 is given by

$$f_{r,z}(r, z) = \frac{3r}{H_2 R^2}, (r, z) \in \{\mathcal{D}_{sc}\}. \qquad (6)$$

where the set $\mathcal{D}_{sc}$ is defined as the union of two discrete subsets, corresponding to the cone which is formed from the center of the sphere and the base of the spherical cap and the cap itself, respectively:

$$\mathcal{D}_{sc} = \left\{ (r, z) \; \middle| \; \begin{array}{l} 0 \le r \le za/H_1, \\ 0 \le z \le H_1, \end{array} \right\}$$
$$\cup \left\{ (r, z) \; \middle| \; \begin{array}{l} 0 \le r \le \sqrt{R^2 - z^2}, \\ H_1 \le z \le R. \end{array} \right\} \qquad (7)$$

Proof: The proof is provided in Appendix A. ∎

B. CHANNEL GAIN DISTRIBUTION

Next, we investigate the stochastic channel gain, h, which corresponds to the random distance d from the axis origin, O, to the reference point, P, as indicated in Fig. 1. The CDF of h can be evaluated as

$$F_h(h) = P\left(h(r, z) \le h\right) = \iint_{\mathcal{D}_h} f_{r,z}(r, z)\, dr dz, \qquad (8)$$

where $\mathcal{D}_h = \{(r, z) \in R^2 : h(r, z) \le h\}$. The final closed-form expression occurs according to Theorem 1.

Theorem 1: The CDF of the channel gain, h, from the axis origin to a random point inside the spherical cone of Fig. 1 is expressed by

$$F_h(h) = \begin{cases} 1 + \dfrac{H_1^2 z^{*3}(h) - R^2 z_{min}^3(h)}{2H_1^2 H_2 R^2} \\ \quad - \mathcal{C}_1 \Lambda_1(h) h^{\frac{1}{m+1}}, & h^{(1)} \le h < h_{max} \\[2em] \dfrac{-2H_1^3 + 3z_{max}(h)H_1^2 - z_{min}^3(h)}{2H_2 H_1^2} \\ \quad - \mathcal{C}_1 \Lambda_2(h) h^{\frac{1}{m+1}}, & h_{min} \le h < h^{(1)} \end{cases}$$
$$(9)$$

where $\mathcal{C}_1 = \dfrac{3(m+3)^{\mu_1}}{4(m+1)H_2R^2c_{av}^{\mu_2}(\lambda, R)\mathcal{B}^{1/(m+1)}}$, $\mathcal{B} = \dfrac{(m+1)A_{PD}T_s(\psi)n^2}{2\pi \sin^2(\phi_{FoV})}$, $\mu_1 = \dfrac{4m+6}{m+1}$, and $\mu_2 = \dfrac{3m+5}{m+1}$, are system-dependent constants. Furthermore, $h_{max} \to \infty$, $h^{(1)} = \dfrac{\mathcal{B}e^{-c_{av}(\lambda, R)R}}{R^2}$, $h_{min} = \dfrac{\mathcal{B}e^{-c_{av}(\lambda, R)R}H_1^{m+1}}{R^{m+3}}$, whereas

$$\Lambda_1(h) = \Lambda\left(3, \frac{Rc_{av}(\lambda, R)z_{min}(h)}{2H_1}, \frac{c_{av}(\lambda, R)z^*(h)}{2}\right)$$
$$+ \Lambda\left(4, \frac{Rc_{av}(\lambda, R)z_{min}(h)}{2H_1}, \frac{c_{av}(\lambda, R)z^*(h)}{2}\right), \quad (10)$$

and

$$\Lambda_2(h) = \Lambda\left(3, \frac{Rc_{av}(\lambda, R)z_{min}(h)}{2H_1}, \frac{\mathcal{C}_2(m+3)}{2}\right)$$
$$+ \Lambda\left(4, \frac{Rc_{av}(\lambda, R)z_{min}(h)}{2H_1}, \frac{\mathcal{C}_2(m+3)}{2}\right), \quad (11)$$

are defined through the user-defined function

$$\Lambda(x, y_1, y_2) = 2(-\mu_3)^{-(x+\frac{2}{m+1})}$$
$$\times \left(\Gamma\left(x + \frac{2}{m+1}, -\frac{2y_1}{m+1}\right)\right.$$
$$\left.- \Gamma\left(x + \frac{2}{m+1}, -\frac{2y_2}{m+1}\right)\right), \quad (12)$$

where $\mu_3 = \dfrac{m+3}{m+1}$, $\mathcal{C}_2 = \dfrac{Rc_{av}(\lambda, R)}{m+3}$ is a system-dependent constant and $\Gamma(\cdot, \cdot)$ is the incomplete Gamma function [26, eq. 06.06.02.0001.01].

Proof: The CDF of h is deduced in Appendix B which also defines and derives $z^*(h)$, $z_{min}(h)$, and $z_{max}(h)$. ∎

The PDF of h is obtained as

Corollary 1: The PDF of the channel gain, h, is expressed by

$$f_h(h) = \begin{cases} \dfrac{3\left(H_1^2 z^{*3}(h) - R^2 z_{min}^3(h)\right)}{2H_1^2H_2R^2(m+1)}h^{-1} - \\ \dfrac{\mathcal{C}_1\Lambda_1(h)}{m+1}h^{-\frac{m}{m+1}}, \qquad h^{(1)} \le h < h_{max} \\ \\ -\dfrac{3z_{min}^3(h)}{2H_1^2H_2(m+1)}h^{-1} + \\ \left(\dfrac{3\mathcal{C}_3}{2H_2(m+1)} - \dfrac{\mathcal{C}_1\Lambda_2(h)}{m+1}\right)h^{-\frac{m}{m+1}}, \\ \qquad h_{min} \le h < h^{(1)} \end{cases} \quad (13)$$

where $\mathcal{C}_3 = \left(\dfrac{R^{m+3}}{\mathcal{B}e^{-Rc_{av}(\lambda, R)}}\right)^{\frac{1}{m+1}}$ is a system-dependent constant.

Proof: The PDF occurs by taking the derivative of (9) with respect to h and applying some simple differentiation rules. ∎

C. SNR DISTRIBUTION

The instantaneous electrical SNR assuming IM/DD at the Rx is defined as $\gamma = \dfrac{(\rho h P_t)^2}{N_0 B} = \gamma_t h^2$, where P_t is the transmitted optical power, ρ is the optical to electrical conversion efficiency, N_0 is the one-sided noise power spectral density of the additive white Gaussian noise (AWGN) term with zero mean and variance of σ_n^2, B is the modulation bandwidth, and $\gamma_t = \dfrac{(\rho P_t)^2}{N_0 B}$ is the SNR at the Tx [13]. The SNR CDF and PDF are given according to Theorem 2 and Corollary 2, respectively.

Theorem 2: The CDF of the instantaneous SNR, γ, is expressed by

$$F_\gamma(\gamma) = \begin{cases} 1 + \dfrac{H_1^2 z^{*3}\left(\sqrt{\frac{\gamma}{\gamma_t}}\right) - R^2 z_{min}^3\left(\sqrt{\frac{\gamma}{\gamma_t}}\right)}{2H_1^2H_2R^2} \\ - \dfrac{\mathcal{C}_1\Lambda_1\left(\sqrt{\frac{\gamma}{\gamma_t}}\right)}{\gamma_t^{\frac{1}{2m+2}}}\gamma^{\frac{1}{2m+2}}, \qquad \gamma^{(1)} \le \gamma < \gamma_{max} \\ \\ \dfrac{-2H_1^3 + 3H_1^2 z_{max}\left(\sqrt{\frac{\gamma}{\gamma_t}}\right) - z_{min}^3\left(\sqrt{\frac{\gamma}{\gamma_t}}\right)}{2H_1^2H_2} \\ - \dfrac{\mathcal{C}_1\Lambda_2\left(\sqrt{\frac{\gamma}{\gamma_t}}\right)}{\gamma_t^{\frac{1}{2m+2}}}\gamma^{\frac{1}{2m+2}}, \qquad \gamma_{min} \le \gamma < \gamma^{(1)} \end{cases}$$
$$(14)$$

where $\gamma^{(1)} = \gamma_t h^{(1)2}$, $\gamma_{max} = \gamma_t h_{max}^2$, and $\gamma_{min} = \gamma_t h_{min}^2$.

Proof: The expression (14) is derived from (9) according to

$$F_\gamma(\gamma) = P(\gamma_t h^2 \le \gamma)$$
$$= P\left(h \le \sqrt{\frac{\gamma}{\gamma_t}}\right) = F_h\left(\sqrt{\frac{\gamma}{\gamma_t}}\right), \quad (15)$$
∎

Corollary 2: The PDF of the instantaneous SNR is expressed by

$$f_\gamma(\gamma) = \begin{cases} \dfrac{3\left(H_1^2 z^{*3}\left(\sqrt{\frac{\gamma}{\gamma_t}}\right) - R^2 z_{min}^3\left(\sqrt{\frac{\gamma}{\gamma_t}}\right)\right)}{4H_1^2H_2R^2(m+1)}\gamma^{-1} \\ - \dfrac{\mathcal{C}_1\Lambda_1\left(\sqrt{\frac{\gamma}{\gamma_t}}\right)}{2\gamma_t^{\frac{1}{2m+2}}(m+1)}\gamma^{-\frac{2m+1}{2m+2}}, \quad \gamma^{(1)} \le \gamma < \gamma_{max} \\ \\ -\dfrac{3z_{min}^3\left(\sqrt{\frac{\gamma}{\gamma_t}}\right)}{4H_1^2H_2(m+1)}\gamma^{-1} + \\ \left(\dfrac{3\mathcal{C}_3}{4H_2\gamma_t^{\frac{1}{2m+2}}(m+1)} - \right. \\ \left. \dfrac{\mathcal{C}_1\Lambda_2\left(\sqrt{\frac{\gamma}{\gamma_t}}\right)}{2\gamma_t^{\frac{1}{2m+2}}(m+1)}\right)\gamma^{-\frac{2m+1}{2m+2}}, \quad \gamma_{min} \le \gamma < \gamma^{(1)} \end{cases}$$
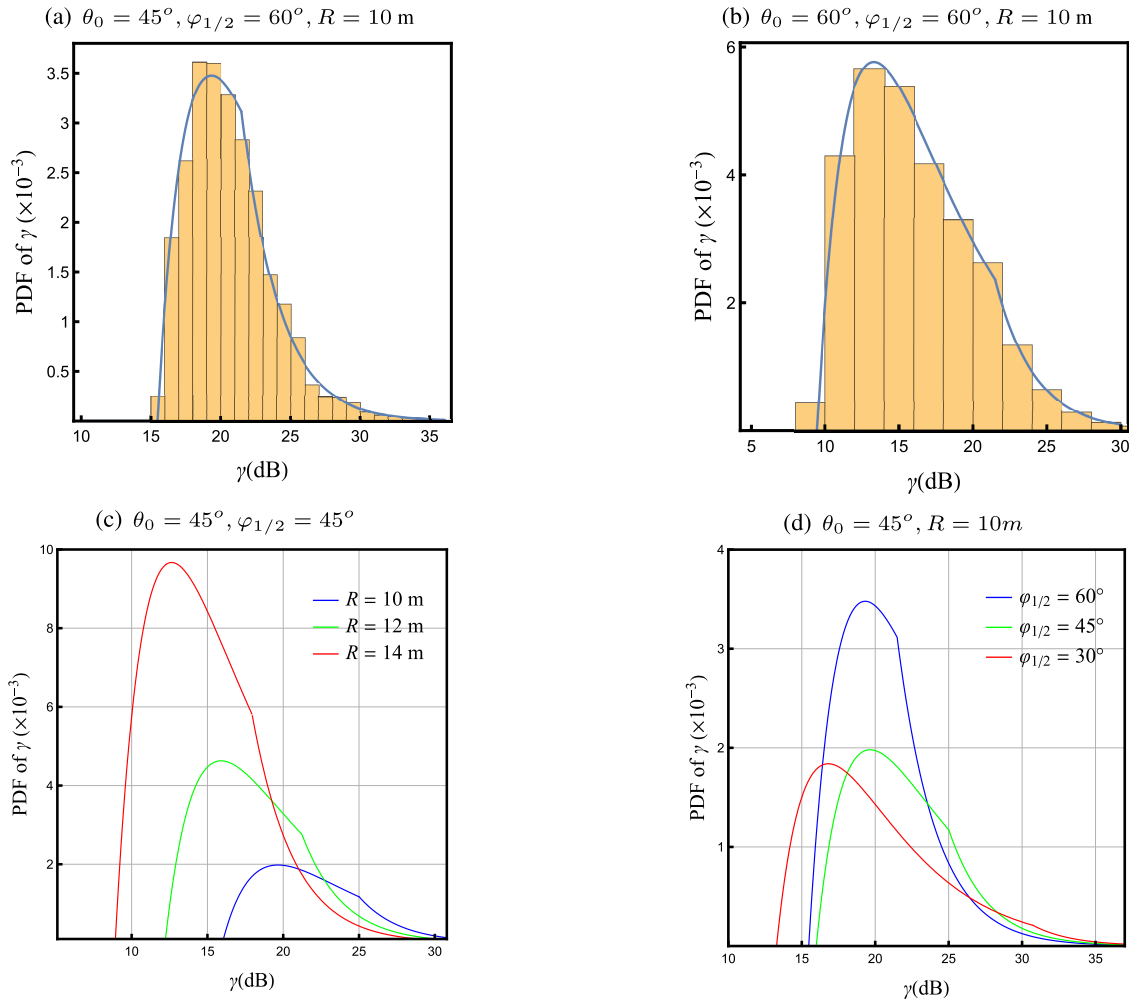$$(16)$$

(a) $\theta_0 = 45^o, \varphi_{1/2} = 60^o, R = 10$ m

(b) $\theta_0 = 60^o, \varphi_{1/2} = 60^o, R = 10$ m

(c) $\theta_0 = 45^o, \varphi_{1/2} = 45^o$

(d) $\theta_0 = 45^o, R = 10m$

FIGURE 3. SNR PDFs for typical values of θ_0, R, and $\varphi_{1/2}$. Histogram corresponds to MC simulation.

Proof: The PDF yields by differentiating (14) with respect to γ. ∎

Some indicative SNR PDF illustrations are demonstrated in Fig. 3 against several parameters. At first, the impact of θ_0 is exhibited in Figs. 3 (a) and (b). We observe that the range of SNR values widens towards lower values as θ_0 gets high. The validity of analytical expressions is enhanced through MC simulation, indicating a satisfactory agreement. On the other hand, the effect of R and $\varphi_{1/2}$ is displayed in Figs. 3 (c) and (d), respectively. Apparently, as R increases, the SNR reduces; so the PDF shifts to lower values. Furthermore, as $\varphi_{1/2}$ deviates and no longer equals θ_0, the SNR also decreases, resulting in a PDF shift towards lower values.

IV. PERFORMANCE METRICS AND RESULTS

In this section, we offer results for two characteristic system performance metrics: the outage probability and the average BER for OOK and M-PPM schemes for two representative chlorophyll profiles, S2 and S5, which have small and moderate values of the average extinction coefficient, respectively.

TABLE 1. Parameter values.

Parameter	Value
Receiver effective area, A_r	$5 \cdot 10^{-5}$ m^2
Refractive index, n	1.33
Receiver Field of View, φ_{FoV}	60°
White noise power spectral density, N_0	10^{-22} W/Hz
Optical to electrical conversion efficiency, ρ	0.9
Rx modulation bandwidth, B	1 Mbps
Operating wavelength, λ	532 nm
SNR at the Tx, γ_t	153 dB
Filter transmission, $T_s(\psi)$	1
$c_{\text{av}}(\lambda, R)$ (S2 profile, $R=\{10, 20, 30\}$ m)	$\{0.0352, 0.0348, 0.0344\}$
$c_{\text{av}}(\lambda, R)$ (S5 profile, $R=\{10, 20, 30\}$ m)	$\{0.0698, 0.0683, 0.0667\}$

Unless specified otherwise, the model parameters used are listed in Table 1 [20], [27].

A. OUTAGE PROBABILITY
Figures 4 and 5 illustrate the outage probability, obtained as $P_{\text{out}} = F_\gamma(\gamma_{\text{th}})$, against the threshold γ_{th} and the values of m,
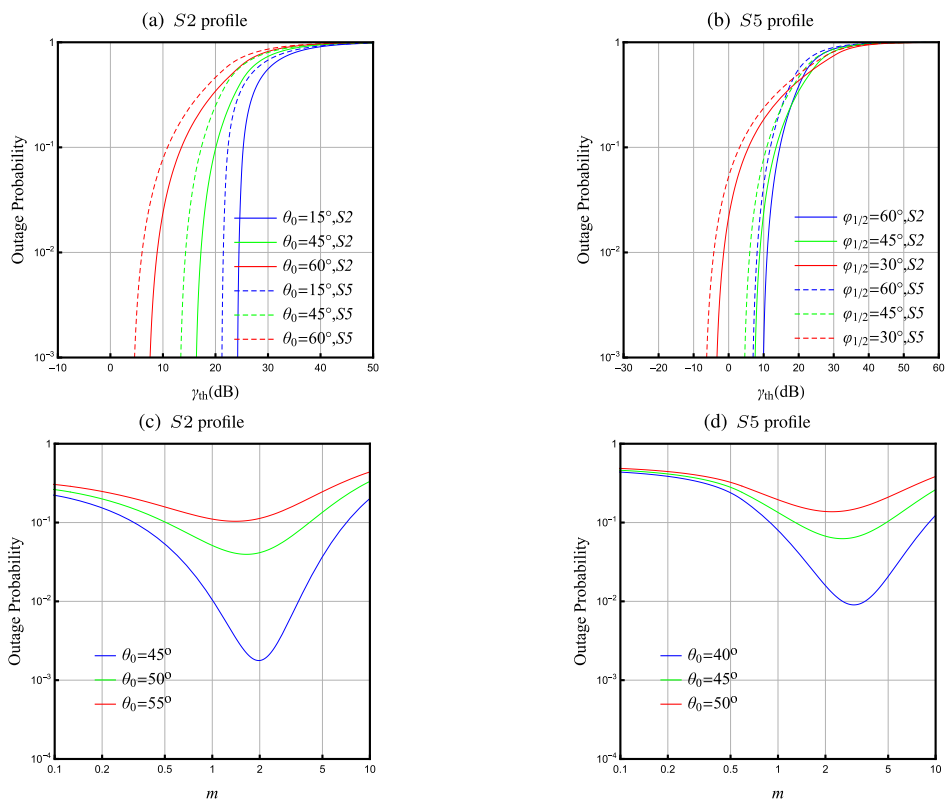
FIGURE 4. Outage probability against γ_{th} and m, for $S2$ and $S5$ chlorophyll profiles.
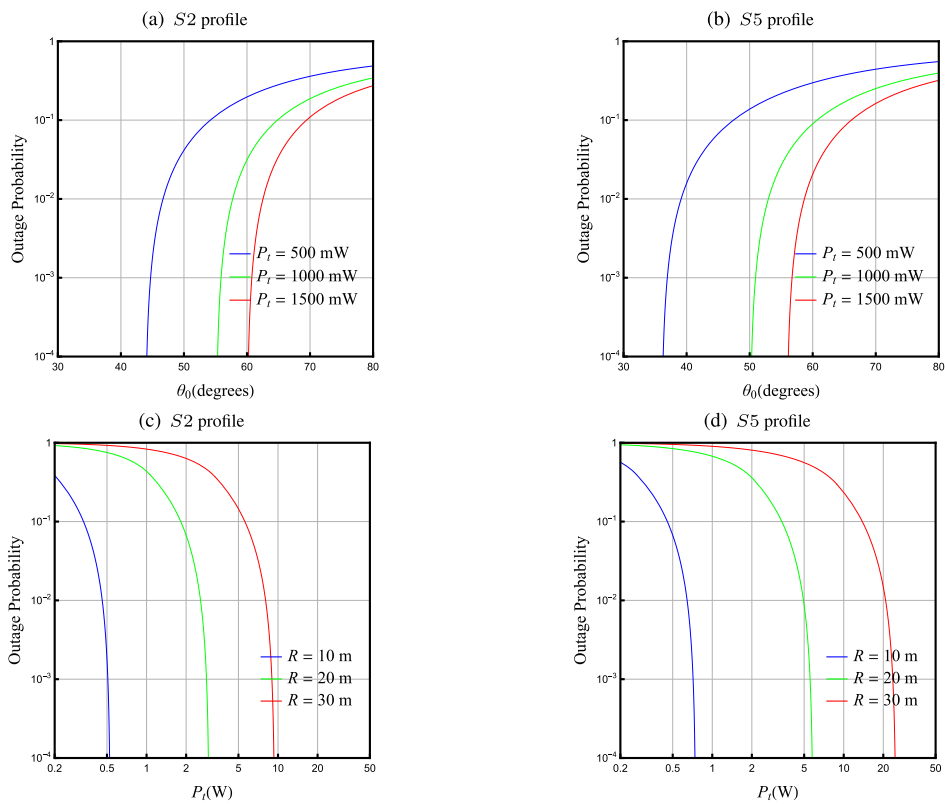

FIGURE 5. Outage probability against θ_0 and P_t for $S2$ and $S5$ chlorophyll profiles.
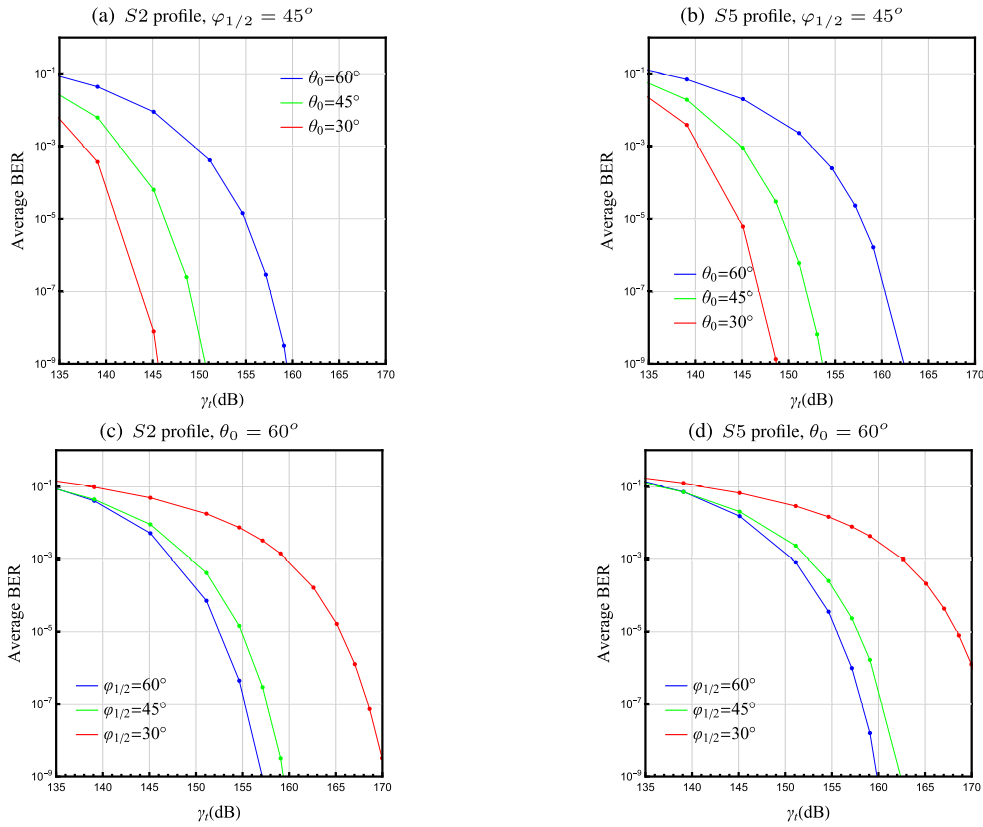
FIGURE 6. Average BER for *S2* and *S5* chlorophyll profiles.

θ_0 and P_t, respectively, for both chlorophyll profiles. Unless specified otherwise, the following parameters are selected: $\theta_0 = 60^o$, $\varphi_{1/2} = 45^o$, $\gamma_{th} = 16.5$ dB and $R = 10$ m. It is clear from Figs. 4 (a) and (b) that P_{out} is lower for the *S2* profile since the average extinction coefficient is smaller. Moreover, the best performance is attained when the Tx emission semi-angle gets approximately equal to the maximum angle of the spherical cone, i.e., $\varphi_{1/2} \approx \theta_0$, as depicted in Figs. 4 (c) and (d). Note that the Tx optical power is distributed at different angles according to the $\varphi_{1/2}$ value. When $\varphi_{1/2}$ is small, the Tx optical power is gathered over smaller angles close to the spherical cone axis. As a result, a greater number of locations within the spherical cone will experience a decrease in optical power. Furthermore, when $\varphi_{1/2}$ is large, the optical power is distributed uniformly over an extensive range of angles, and therefore locations within the spherical cone will again receive less optical power. Finally, it should also be noted that the optimal value of $\phi_{1/2}$ changes slightly from profile *S2* to *S5* since the propagation medium becomes more hostile. Thus, its impact on the link performance becomes more decisive.

On the other hand, Figs. 5 (a) and (b) present the trade-off between θ_0 and P_t for a required P_{out} value, assuming both chlorophyll profiles. Referring to Fig. 5 (a) for $P_{out} = 10^{-3}$ and $P_t = 500$ mW we achieve $\theta_0 \simeq 45^o$, whereas for $P_t = 1000$ mW θ_0 is approximately 56°. Moreover, for $P_t =$

1500 mW, the value of this angle is about 61°. Similar conclusions can be drawn for the *S5* profile, with the difference that the angles are about 4–7 degrees smaller in each case. Finally, the trade-off between R and P_t for both chlorophyll profiles is visualized in Fig. 5 (c) and (d). Keeping the exact requirement for the P_{out} value and doubling the R value, i.e., from $R = 10$ m to $R = 20$ m, requires a sixfold or eightfold increase in Tx power, correspondingly, for each profile. This is quite an important parameter to consider during the network design process.

B. AVERAGE BER

We consider IM/DD since coherent detection presents technical difficulties, increased cost, and complexity in hostile underwater environments, where scattering and turbulence prevent detection changes of the optical carrier [28]. Another important reason for this choice is that coherent detection schemes can only be achieved with coherent sources, e.g., collimated laser sources, and not incoherent ones like LEDs [29]. In this vein, we select OOK and M-PPM as the most appropriate modulation schemes to calculate the average BER, according to the following expressions [20], [30]

$$P_e^{\text{OOK}} = \frac{1}{2} \int_{\gamma_{\min}}^{\gamma_{\max}} \text{erfc}\left(\sqrt{\frac{\gamma}{2}}\right) f_\gamma(\gamma) d\gamma, \tag{17}$$
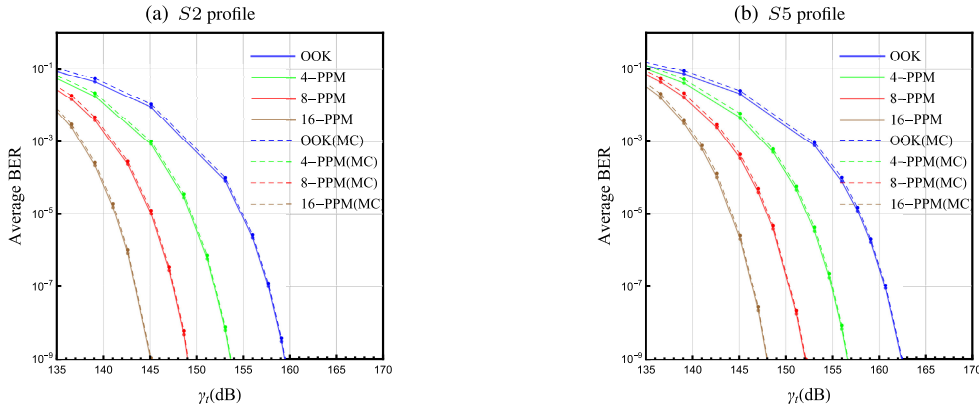
FIGURE 7. Average BER for $S2$ and $S5$ chlorophyll profiles, considering two modulation schemes.
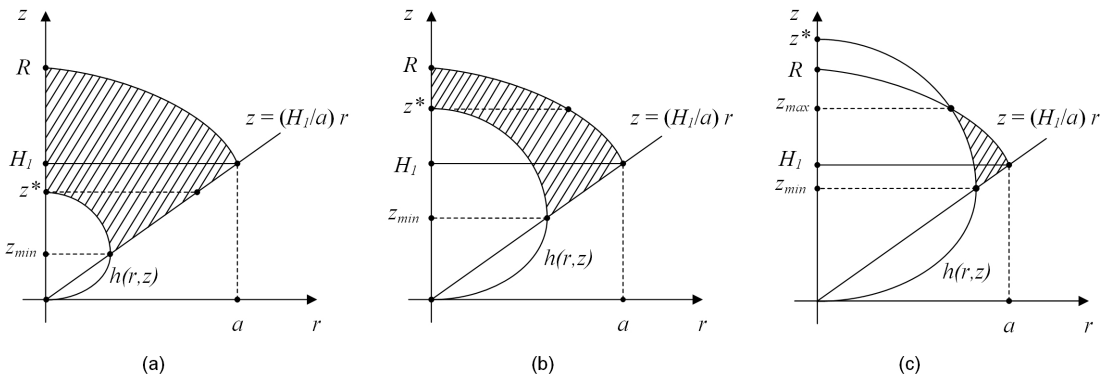

FIGURE 8. Areas for the surface integral evaluation in (8).

$$P_e^{M-\text{PPM}} = \frac{M}{4} \int_{\gamma_{\min}}^{\gamma_{\max}} \text{erfc}\left(\sqrt{\frac{\gamma M \log_2 M}{4}}\right) f_\gamma(\gamma) d\gamma, \quad (18)$$

where erfc$(\cdot)$ is the complementary error function [26, eq. 06.27.02.0001.01]. The integrals in (17) and (18) include the Lambert and incomplete Gamma functions and hence cannot be solved analytically but numerically.

Figures 6 and 7 demonstrate the average BER against γ_t, for both chlorophyll profiles, assuming several θ_0 values (Fig. 6 (a) and (b)), $\varphi_{1/2}$ (Fig. 6 (c) and (d)) as well as the two modulation schemes (Fig. 7 (a) and (b)), accordingly. It can be witnessed in Fig. 6 (a) and (b) that for given $\varphi_{1/2}$ and γ_t values, the average BER degrades as θ_0 increases since the SNRs at the potential Rx positions are low. For instance, reffering to the $S2$ profile and for a value of γ_t equal to 145 dB, the average BER raises from $7 \cdot 10^{-9}$ to $6 \cdot 10^{-5}$ as the angle θ_0 widens from 30 to 45 degrees. If θ_0 increases to 60 degrees, the average BER becomes equal to 10^{-2}. Furthermore, in order to achieve an average BER of 10^{-6}, the required γ_t value increases, for both profiles, by 5 dB as the angle θ_0 widens from 30 to 45 degrees. An additional 8 dB is required as θ_0 increases from 45 to 60 degrees. In Fig. 6 (c) and (d), we observe similar behavior to the outage probability. Indeed, we notice that the optimum average BER

performance is attained when the semi-angle value is approximately equal to θ_0, whereas a possible reduction of this angle leads to worse average BER results. Finally, in Fig. 7 (a) and (b), we observe the predominance of M-PPM schemes over OOK. Assuming $P_e = 10^{-5}$, the difference between 16-PPM and 8-PPM, as well as 8-PPM and 4-PPM is about 4 dB, whereas the difference between 4-PPM and OOK is about 6 dB. The numerical results have been validated through MC simulation results, where 10^3 samples were generated, and the observed level of agreement is satisfactory.

V. CONCLUSION AND FURTHER RESEARCH

The location uncertainty issue in a spherical conical volume was adequately addressed from the stochastic geometry viewpoint. The problem is quite attractive and applies to UOWC connections where an Rx is often located at a random position inside the covering volume of such a shape served by a Tx that radiates with a Lambertian pattern. Using an appropriate methodological framework, we derived closed-form expressions for the distributions that fully describe the channel gain and instantaneous electrical SNR. These outcomes allow the determination of some primary performance metrics, such as the outage probability and the average BER for OOK and M-

PPM assuming IM/DD. Moreover, MC simulations are used for validation.

In the current study, the user is assumed to be stationary at a given location. Any slight movement or swinging around its position would make the analysis extremely difficult since the corresponding randomness of movement must be determined and incorporated along with the position uncertainty. For example, employing the commonly used random waypoint model (RWP) for large movements within the conical volume requires the extraction of a complicated joint PDF instead of (6). On the other hand, adopting any small oscillatory moves demands the inclusion of an additional impairment in the analysis. Such extensions would lead to complicated equations that could not be solved analytically. Thus, the problem of considering small or large motion effects is left as a possible future extension. Furthermore, different channel conditions (such as salinity, temperature, etc.) can be investigated by adequately adjusting the value of the average extinction coefficient.

The authors will exceptionally be satisfied if their findings resonate with the scientific community and contribute to solving similar problems commonly encountered in wireless communications using stochastic geometry techniques. As regards UOWC networking, some partial extensions include, among others, the incorporation of other uncertainties such as the capture of solar noise effect, the combined effect of oceanic turbulence and air bubbles, and a multi-user and/or multiple Txs scenarios as described in [25], [31], and [32], respectively. In all these cases, the derivations from this study can be viewed as the initial step toward the performance evaluation of more complicated networking scenarios.

APPENDIX A PROOF OF LEMMA 1

The spherical conical volume is evaluated according to [33, eq. 3.160] as

$$V = \frac{2\pi R^2 H_2}{3}. \tag{A.1}$$

Therefore, the uniformly located point, P, is determined in Cartesian coordinates by the joint PDF of

$$f_{x,y,z}(x, y, z) = \begin{cases} \frac{1}{V}, & H_1^2 x^2 + H_1^2 y^2 \le a^2 z^2, 0 \le z \le H_1 \\ \frac{1}{V}, & x^2 + y^2 \le R^2 - z^2, H_1 \le z \le R \\ 0, & else, \end{cases} \tag{A.2}$$

By converting to cylindrical coordinates using $x = r\cos\theta, y = r\sin\theta, z = z$, we arrive at

$$f_{r,\theta,z}(r, \theta, z) = \frac{f_{x,y,z}(x, y, z)}{|J(x, y, z)|}. \tag{A.3}$$

Eq. (6) eventually occurs if we replace the Jacobian $|J(x, y, z)| = \frac{1}{r}$ into (A.3) and notice that θ is an independent uniformly distributed random variable with $f_\theta(\theta) = \frac{1}{2\pi}$.

APPENDIX B PROOF OF THEOREM 1

In order to solve the surface integral in (8), we distinguish three different cases where area, $\mathcal{D}_h$, satisfies the condition $P(h(r, z) \le h)$. These cases are clearly shown in Fig. 8.

For each case we determine some necessary critical points in order to solve the integrals. At first, we consider the intersection of the z-axis with the curve

$$h(r, z) = \mathcal{B}(r^2 + z^2)^{-\frac{m+3}{2}} z^{m+1} e^{-c_{av}(\lambda, R)\sqrt{r^2+z^2}}. \tag{B.1}$$

After some algebra, this point is determined as

$$z^*(h) = \frac{2}{c_{av}(\lambda, R)} W_0\left(\frac{c_{av}(\lambda, R)}{2}\sqrt{\frac{\mathcal{B}}{h}}\right). \tag{B.2}$$

where $W_0(\cdot)$ is the principal branch of the Lambert function [26, eq. 01.31.02.0001.01]. Then, we consider the projections, $z_{min}(h)$ and $z_{max}(h)$, on z-axis of the intersection of this curve with the line $z = \frac{H_1}{a}r$ and the circle $r^2 + z^2 = R^2$, accordingly as

$$z_{min}(h) = \frac{2H_1}{c_{av}(\lambda, R)R} W_0\left(\frac{c_{av}(\lambda, R)}{2}\sqrt{\frac{\mathcal{B}}{h}\left(\frac{H_1}{R}\right)^{m+1}}\right), \tag{B.3}$$

$$z_{max}(h) = \mathcal{C}_3 h^{1/(m+1)}. \tag{B.4}$$

After we have identified these points, we proceed to define the integration limits for each area as

$$F_h(h) = \begin{cases} \int_{z_{min}}^{z^*}\int_{r(z)}^{\frac{z\alpha}{H_1}} f_{r,z}(r, z)\,dr\,dz + \\ \int_{z^*}^{H_1}\int_0^{\frac{z\alpha}{H_1}} f_{r,z}(r, z)\,dr\,dz + \\ \int_{H_1}^{R}\int_0^{\sqrt{R^2-z^2}} f_{r,z}(r, z)\,dr\,dz, & h^{(2)} \le h < h_{max} \\ \\ \int_{z_{min}}^{H_1}\int_{r(z)}^{\frac{z\alpha}{H_1}} f_{r,z}(r, z)\,dr\,dz + \\ \int_{H_1}^{z^*}\int_0^{\frac{z\alpha}{H_1}} f_{r,z}(r, z)\,dr\,dz + \\ \int_{z^*}^{R}\int_0^{\sqrt{R^2-z^2}} f_{r,z}(r, z)\,dr\,dz, & h^{(1)} \le h < h^{(2)} \\ \\ \int_{z_{min}}^{H_1}\int_{r(z)}^{\frac{z\alpha}{H_1}} f_{r,z}(r, z)\,dr\,dz + \\ \int_{H_1}^{z_{max}}\int_{r(z)}^{\sqrt{R^2-z^2}} f_{r,z}(r, z)\,dr\,dz, & h_{min} \le h < h^{(1)}. \end{cases} \tag{B.5}$$

where $h^{(2)} = \dfrac{\mathcal{B}e^{-c_{av}(\lambda, R)H_1}}{H_1^2}$ and $r(z)$ is the solution of (3) with respect to r after substituting $\cos(\varphi) = \sqrt{r^2 + z^2}/z$ and

$d = \sqrt{r^2 + z^2}$, i.e.,

$$r(z) = \sqrt{\left(\frac{m+3}{c_{av}(\lambda, R)}\right)^2 W_0^2 \left(\frac{c_{av}(\lambda, R)}{m+3} \left(\frac{\mathcal{B}}{h}\right)^{\frac{1}{m+3}} z^{\mu_3}\right) - z^2}.$$
(B.6)

In order to proceed with our analysis, we substitute (6) into (B.5), and then solve the resulting double integrals individually. It is noteworthy that the first two branches of (B.5) are equivalent in terms of their outcome. As a result, the final expression of (9) contains only two branches.

REFERENCES

[1] Z. Zeng, S. Fu, H. Zhang, Y. Dong, and J. Cheng, "A survey of underwater optical wireless communications," *IEEE Commun. Surveys Tuts.*, vol. 19, no. 1, pp. 204–238, 1st Quart., 2017.

[2] H. Kaushal and G. Kaddoum, "Underwater optical wireless communication," *IEEE Access*, vol. 4, pp. 1518–1547, 2014.

[3] M. F. Ali, D. N. K. Jayakody, and Y. Li, "Recent trends in underwater visible light communication (UVLC) systems," *IEEE Access*, vol. 10, pp. 22169–22225, 2022.

[4] C. Christopoulou, H. G. Sandalidis, and A. Vavoulas, "Optimal trade-off between depth and coverage for a vertical UOWC link," *IEEE Photon. Technol. Lett.*, vol. 32, no. 4, pp. 208–211, Feb. 15, 2020.

[5] I. C. Ijeh, M. A. Khalighi, and S. Hranilovic, "Parameter optimization for an underwater optical wireless vertical link subject to link misalignments," *IEEE J. Ocean. Eng.*, vol. 46, no. 4, pp. 1424–1437, Oct. 2021.

[6] Y. Weng, T. Matsuda, Y. Sekimori, J. Pajarinen, J. Peters, and T. Maki, "Pointing error control of underwater wireless optical communication on mobile platform," *IEEE Photon. Technol. Lett.*, vol. 34, no. 13, pp. 699–702, Jul. 1, 2022.

[7] H. M. Oubei, R. T. ElAfandy, K.-H. Park, T. K. Ng, M.-S. Alouini, and B. S. Ooi, "Performance evaluation of underwater wireless optical communications links in the presence of different air bubble populations," *IEEE Photon. J.*, vol. 9, no. 2, pp. 1–9, Apr. 2017.

[8] Y. Dong, S. Tang, and X. Zhang, "Effect of random sea surface on downlink underwater wireless optical communications," *IEEE Commun. Lett.*, vol. 17, no. 11, pp. 2164–2167, Nov. 2013.

[9] R. Boluda-Ruiz, P. Salcedo-Serrano, B. Castillo-Vázquez, A. García-Zambrana, and J. M. Garrido-Balsells, "Capacity of underwater optical wireless communication systems over salinity-induced oceanic turbulence channels with ISI," *Opt. Exp.*, vol. 29, no. 15, p. 23142, Jul. 2021.

[10] E. Zedini, H. M. Oubei, A. Kammoun, M. Hamdi, B. S. Ooi, and M.-S. Alouini, "Unified statistical channel model for turbulence-induced fading in underwater wireless optical communication systems," *IEEE Trans. Commun.*, vol. 67, no. 4, pp. 2893–2907, Apr. 2019.

[11] Y. Lou, J. Cheng, D. Nie, and G. Qiao, "Performance of vertical underwater wireless optical communications with cascaded layered modeling," *IEEE Trans. Veh. Technol.*, vol. 71, no. 5, pp. 5651–5655, May 2022.

[12] A. Celik, N. Saeed, B. Shihada, T. Y. Al-Naffouri, and M.-S. Alouini, "End-to-end performance analysis of underwater optical wireless relaying and routing techniques under location uncertainty," *IEEE Trans. Wireless Commun.*, vol. 19, no. 2, pp. 1167–1181, Feb. 2020.

[13] C. Christopoulou, H. G. Sandalidis, and N. Vaiopoulos, "Performance of an underwater optical wireless link with a randomly placed or moving receiver," *IEEE J. Ocean. Eng.*, vol. 46, no. 3, pp. 1068–1079, Jul. 2021.

[14] S. N. Chiu, D. Stoyan, W. S. Kendall, and J. Mecke, *Stochastic Geometry and Its Applications*. Hoboken, NJ, USA: Wiley, 2013.

[15] A. M. Mathai, *An Introduction to Geometrical Probability: Distributional Aspects With Applications*. Amsterdam, The Netherlands: Gordon & Breach, 1999.

[16] P. K. Sharma and D. I. Kim, "Random 3D mobile UAV networks: Mobility modeling and coverage probability," *IEEE Trans. Wireless Commun.*, vol. 18, no. 5, pp. 2527–2538, May 2019.

[17] A. Talgat, M. A. Kishk, and M.-S. Alouini, "Nearest neighbor and contact distance distribution for binomial point process on spherical surfaces," *IEEE Commun. Lett.*, vol. 24, no. 12, pp. 2659–2663, Dec. 2020.

[18] N. Okati, T. Riihonen, D. Korpi, I. Angervuori, and R. Wichman, "Downlink coverage and rate analysis of low Earth orbit satellite constellations using stochastic geometry," *IEEE Trans. Commun.*, vol. 68, no. 8, pp. 5120–5134, Aug. 2020.

[19] N. Vaiopoulos, A. Vavoulas, and H. G. Sandalidis, "Exploring the random location problem inside a truncated conic shape: Application in UAV communications," *IEEE Trans. Commun.*, vol. 70, no. 4, pp. 2882–2890, Apr. 2022.

[20] N. Vaiopoulos, A. Vavoulas, and H. G. Sandalidis, "Impact of a randomly placed terminal on LiFi performance," *IEEE Trans. Commun.*, vol. 70, no. 3, pp. 1875–1885, Mar. 2022.

[21] C. T. Nguyen, V. V. Mai, and C. T. Nguyen, "Probing packet retransmission scheme in underwater optical wireless communication with energy harvesting," *IEEE Access*, vol. 9, pp. 34287–34297, 2021.

[22] V. I. Haltrin, "Chlorophyll-based model of seawater optical properties," *Appl. Opt.*, vol. 38, no. 33, pp. 6826–6832, 1999.

[23] C. Mobley, *Light and Water: Radiative Transfer in Natural Waters*. New York, NY, USA: Academic, 1994.

[24] L. J. Johnson, R. J. Green, and M. S. Leeson, "Underwater optical wireless communications: Depth dependent variations in attenuation," *Appl. Opt.*, vol. 52, no. 33, pp. 7867–7873, 2013.

[25] T. Hamza, M.-A. Khalighi, S. Bourennane, P. Léon, and J. Opderbecke, "Investigation of solar noise impact on the performance of underwater wireless optical communication links," *Opt. Exp.*, vol. 24, no. 22, p. 25832, Oct. 2016.

[26] S. Wolfram. *The Mathematical Functions Site*. Wolfram Research. Accessed: Jul. 8, 2022. [Online]. Available: http://functions.wolfram.com

[27] A. Vavoulas, H. G. Sandalidis, and D. Varoutas, "Underwater optical wireless networks: A K-connectivity analysis," *IEEE J. Ocean. Eng.*, vol. 39, no. 4, pp. 801–809, Oct. 2014.

[28] N. Saeed, A. Celik, T. Y. Al-Naffouri, and M.-S. Alouini, "Underwater optical wireless communications, networking, and localization: A survey," *Ad Hoc Netw.*, vol. 94, Nov. 2019, Art. no. 101935.

[29] X. Tang, R. Kumar, C. Sun, L. Zhang, Z. Chen, R. Jiang, H. Wang, and A. Zhang, "Towards underwater coherent optical wireless communications using a simplified detection scheme," *Opt. Exp.*, vol. 29, no. 13, p. 19340, Jun. 2021.

[30] K. Lee and H. Park, "Modulations for visible light communications with dimming control," *IEEE Photon. Technol. Lett.*, vol. 23, no. 16, pp. 1136–1138, Aug. 15, 2011.

[31] M. V. Jamali, A. Mirani, A. Parsay, B. Abolhassani, P. Nabavi, A. Chizari, P. Khorramshahi, S. Abdollahramezani, and J. A. Salehi, "Statistical studies of fading in underwater wireless optical channels in the presence of air bubble, temperature, and salinity random variations," *IEEE Trans. Commun.*, vol. 66, no. 10, pp. 4706–4723, 2018.

[32] C. Christopoulou, H. G. Sandalidis, and I. S. Ansari, "Outage probability of a multisensor mixed UOWC–FSO setup," *IEEE Sensors Lett.*, vol. 3, no. 8, pp. 1–4, Aug. 2019.

[33] I. N. Bronshtein, K. A. Semendyayev, G. Musiol, and H. Muhlig, *Handbook of Mathematics*, 6th ed. New York, NY, USA: Springer-Verlag, 2015.

NICHOLAS VAIOPOULOS received the B.Sc. degree in physics, the M.Sc. degree in electronics and radio communications, and the Ph.D. degree in optical wireless communications from the University of Athens, Greece, in 2000, 2003, and 2013, respectively. Since 2009, he has been a member of the Laboratory Teaching Staff with the Department of Computer Science and Biomedical Informatics, University of Thessaly, Lamia, Greece. He has authored or coauthored more than ten publications in refereed journals and conference proceedings. His research interests include transferring and managing broadband traffic in optical wireless telecommunication networks and telecommunication network design.

ALEXANDER VAVOULAS received the B.Sc. degree in physics, the M.Sc. degree in electronics and radio communications, and the Ph.D. degree in optical wireless communications from the University of Athens, Greece, in 2000, 2002, and 2013, respectively. Since 2009, he has been a member of the Laboratory Teaching Staff with the Department of Computer Science and Biomedical Informatics, University of Thessaly, Lamia, Greece. He has participated in many national research projects. He has more than 20 publications in refereed journals and conference proceedings. His research interests include indoor, outdoor, and underwater optical wireless communication systems and networks. He serves as a reviewer for several journals and conferences.

HARILAOS G. SANDALIDIS was born in Florina, Greece, in 1972. He received the five-year Diploma degree in electronics and computer engineering from the Production Engineering and Management Department, Technical University of Crete, Greece, in 1995, the M.Sc. degree in radiofrequency and microwave communications from the Electronics and Telecommunications (former Electronics and Electrical engineering) Department, University of Bradford, U.K., in 1996, the M.Sc. degree in business administration from the Production Engineering and Management Department, Technical University of Crete, in 1998, and the Ph.D. degree in the telecommunications area from the Electronics and Telecommunications (former Electronics and Electrical engineering) Department, University of Bradford, in 2002. He is currently pursuing the Ph.D. degree with the University of Bradford. From 1996 to 2001, he was a Research Assistant with the Telecommunications Systems Institute, Crete, Greece. After his military service, he joined TEMAGON, the technology consulting branch of the Hellenic Telecommunications Organization (OTE Group), in 2002, where he was involved in the risk mitigation program for the 2004 Olympic Telecommunication Network in collaboration with Telcordia Technologies Inc. From 2003 to 2009, he was a Senior Investigator with the Greek Ombudsman Office. In March 2009, he joined the Department of Computer Science and Biomedical Informatics, University of Central Greece, as a Lecturer. He is a Professor with the Department of Computer Science and Biomedical Informatics, which currently belongs to the University of Thessaly. His research interests include optical wireless networking, including free-space optics, underwater optical networks, and visible light communications.

HECTOR E. NISTAZAKIS was born in Athens, Greece. He received the B.Sc., M.Sc., and Ph.D. degrees, in 1997, 1999, and 2002, respectively. He is currently a Professor of electronic physics, the Chair of the Department of Physics, National and Kapodistrian University of Athens, and the Director of the Laboratory of Physics. He has authored or coauthored more than 240 journal articles and conference papers, 13 book chapters, and two books. His current research interests include optical communication systems, wireless communications, FSO links, UOWC systems, VLC, nonlinear dynamics, analog and digital circuits and systems, nonlinear circuits and systems, and computational methods in telecommunications and physics. He acts as an associate editor or a guest editor of six international scientific journals, as a TPC member of more than 30 international conferences, and as an organizing committee in five conferences.

ATHANASIOS (THANOS) KAKAROUNTAS (Senior Member, IEEE) is currently an Associate Professor of embedded computing systems with the Department of Computer Science and Biomedical Informatics, University of Thessaly. He is also the Head of the Intelligent Systems Laboratory and the Deputy Chairman of the National Infrastructures for Research and Technology. He has participated in more than 25 research projects and published more than 120 papers in international journals and conference proceedings. His research interests include reconfigurable computing, embedded systems design for the IoT, health, smart cities, and security applications. He is elected to the Board of the IEEE Greece Section and is the Co-Chair of the eGOV Special Technical Committee, IEEE Computer Society. He has served as the Chair for the Research and Innovation Regional Committee for the Region of Central Greece. He was the Interim Chairman of the Consumer Electronics Society-Greece Chapter.

● ● ●